ACS OMEGA

http://pubs.acs.org/journal/acsodf

Article

Reducing Frost during Cryoimaging Using a Hygroscopic Ice Frame

Adam W. Lowery, Ashwin Ambi, Lisa M. Miller, and Jonathan B. Boreyko*

Cite This: *ACS Omega* 2022, 7, 43421−43431

Read Online

ACCESS | Metrics & More | Article Recommendations | Supporting Information

ABSTRACT: Cryomicroscopy is commonly hampered by frost accumulation, reducing the visual clarity of the specimen. Pulling a vacuum or purging with nitrogen gas can greatly reduce the sample chamber's humidity, but at cryogenic temperatures, even minute concentrations of water vapor can still result in frost deposition. Here, a hygroscopic ice frame was created around the specimen to suppress frost growth during cryomicroscopy. Specifically, fluorescently tagged rat brain vessels were frozen on a silicon nitride window with an ice frame, and the luminescence of the fluorescent tag was improved by a factor of 6 compared to a similar specimen in only a nitrogen purge environment. These findings suggest that the simple implementation of a hygroscopic ice frame surrounding the specimen can substantially improve the visual clarity for cryomicroscopy, beyond that of a vacuum or nitrogen purge system.

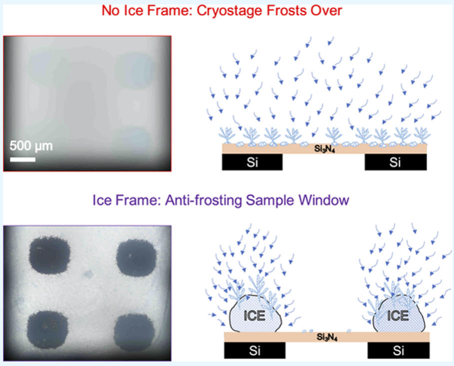

■ INTRODUCTION

Cryomicroscopy is an increasingly common technique for characterizing the nano/microstructures of hydrated, biological specimens using techniques such as X-ray and electron microscopies. Cryogenically freezing the specimen is important for preserving the hydrated specimen's metabolic/native state.[1] In contrast, other preparation methods have known limitations; for example, dehydration can induce sample shrinkage,[2] and chemical fixation is known to disrupt the organization of cellular structures and may not establish complete immobilization.[3] Cryoimaging of hydrated samples also limits beam damage and phototoxicity.[4,5] The advantages of cryogenic freezing have led to its implementation within the sample preparation and imaging workflows for both X-ray and electron imaging techniques.[6−8] In most cases, imaging a frozen, hydrated specimen requires the support of a cryostage to maintain its cryogenic environment.[9] The specimen is best held in a very specific temperature region ($T \leq 135$ K) to maintain a vitreous ice environment; increasing above this glass-transition temperature results in the formation of crystalline ice and damage to the cellular structure of the specimen.[10−12]

A cryostage maintains an environment devoid of water vapor and condensable gases by either pulling a vacuum or using a dry gas purge.[13,14] However, despite the dry environment, trace levels of condensable water vapor can still accumulate on the sample as frost. Frost accumulation reduces the visual clarity of the frozen sample, making it difficult to locate and identify notable subcellular structures, especially when imaging the sample at submicron resolution.[15] The accumulation of frost is even more problematic when frozen specimens are examined with multiple imaging modes, i.e., correlative imaging, where the sample is often shifted between multiple viewing media and environments.[16,17] The transfer mechanisms are often inefficient and add humidity to the environment, which then deposits as frost on the sample surface as it acts as a de facto cold trap.

Recently, it has been shown that ice can, ironically, enable a passive antifrosting surface.[18] Analogous to salts,[19] frozen water is hygroscopic,[20] meaning that its saturated vapor pressure is depressed with respect to liquid water at the same temperature. For example, when growing condensation on a substrate that contains a frozen droplet, an intermediate dry zone is sustained about the perimeter of the ice.[21] When patterning an array of microscopic ice features across a surface, these dry zones can overlap, resulting in the antifrosting functionality.[18,22] To date, the use of ice to prevent frost has only been employed for moderately chilled surfaces in a warm ambient environment and has not been tested under cryogenic conditions.

In this article, we show that adding ice to the outer frame of a silicon nitride window can greatly suppress the growth of frost on the surface of the specimen, thereby enhancing the sample clarity during cryogenic imaging (Figure 1). The ice frame will depress the saturation pressure to preferentially attract nearby water vapor away from the frozen sample while maintaining a uniform-temperature stage. This is in contrast to a conventional cold trap (anticontamination device), whose mechanisms rely on low-temperature differentials.[23−25] A black dot array on white paper was used to contrast the clarity of the sample window under various conditions. We found that, after 3 h even without a nitrogen purge, the clarity of the dot array with the ice

Received: May 17, 2022
Accepted: September 13, 2022
Published: November 22, 2022

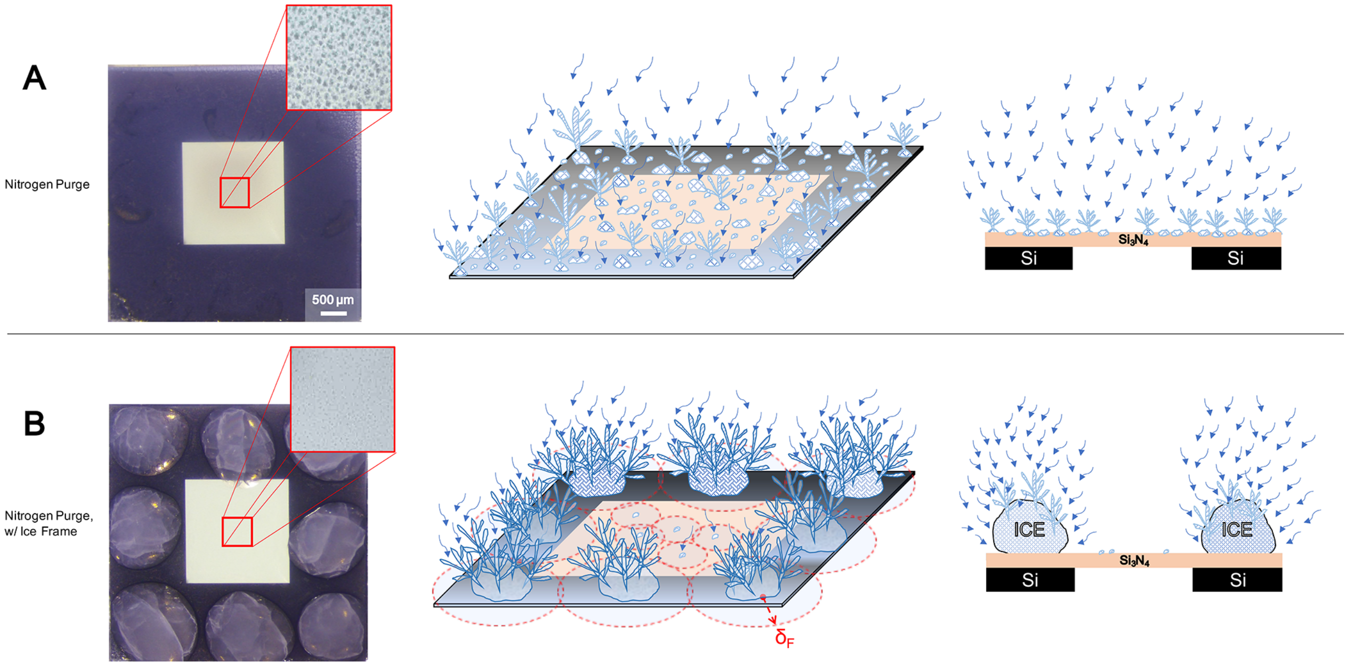

Figure 1. Conceptual overview of using an ice frame to suppress frost during cryomicroscopy. (A) Top-down photograph of the silicon nitride window at cryogenic temperatures within the sample chamber of a nitrogen-purged cryogenic stage. The inset photograph shows the development of frost from residual water vapor on the window after 3 h. The high density of frost obscures the sample visibility on the window. The adjacent drawings are isometric and side-view schematics of diffusive frost growth (blue arrows) on an untreated silicon nitride window. (B) Top-down photograph of the silicon nitride window at cryogenic temperatures within the sample chamber of a nitrogen-purged cryogenic stage. An ice frame is developed on this window frame, along the periphery of the sample substrate edge. The large frozen droplets of the ice frame preferentially attract the surrounding water vapor, resulting in annular dry zones (red circles) of width δ_F. While some water vapor still nucleates as frost on the window, its nucleation density is sparse and the frost dendrites create additional overlapping dry zones. The inset photograph shows the development of frost on the window membrane after 3 h. The adjacent drawings are isometric and side-view schematics of diffusive frost growth (blue arrows) on a silicon nitride window with a hygroscopic ice frame.

frame was twice as good as the dot array without the ice frame. This enhanced clarity enabled continued fluorescence imaging of a biological sample (rat brain blood vessels) on the cryostage, whereas the fluorescence signal almost completely disappeared in the absence of the ice frame. These results clearly showed that using a hygroscopic ice frame to promote antifrosting can be extended to specimens at cryogenic conditions, resulting in a simple and effective technique to improve cryoimaging.

■ RESULTS

Two different sets of cryomicroscopy experiments were performed, each under four different experimental conditions. Both sets of experiments quantify how frost degrades the optical quality of the cryomicroscopy over time, first using a black dot array on white paper and the second, a biological tissue specimen. In either case, the substrate was a silicon nitride window surrounded by a silicon frame. The four different conditions were as follows: (1) no nitrogen purge and no ice frame, (2) nitrogen purge and no ice frame, (3) nitrogen purge with an ice frame, and (4) no nitrogen purge with an ice frame.

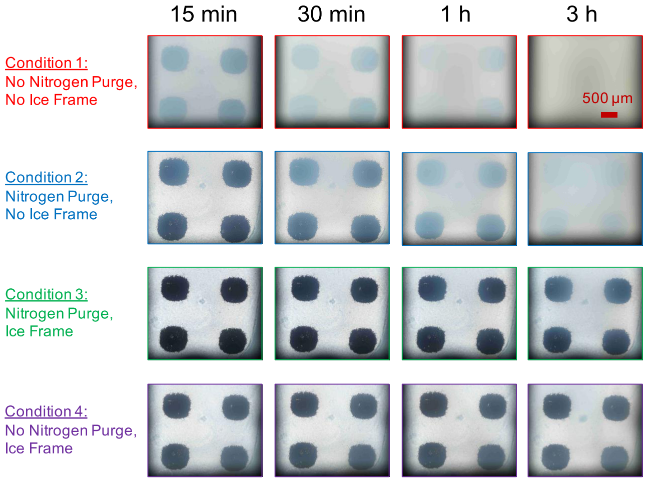

Figure 2. Evolving clarity of dot arrays beneath silicon nitride windows at cryogenic temperatures. Bright-field microscopy was taken in 15 min intervals over the course of 3 h. The dots quickly became obscured in the absence of an ice frame (top row), even with a nitrogen purge (second row). In contrast, dot clarity was largely maintained for windows primed with ice frames (third row), even in the absence of a nitrogen purge (fourth row).

Dot Arrays. The technique of using an underlying black dot array on a white film paper to quantify the clarity of the silicon nitride window was adapted from Walker et al., which used a similar approach for quantifying fogging on transparent surfaces.[15,26] Figure 2 compares the optical microscopy of the cryostage under four different experimental conditions over a span of 3 h. In the absence of an ice frame, frost grows appreciably across the silicon nitride window (Supporting Figure S1), which makes it difficult to resolve the underlying dot array. In contrast, using a hygroscopic ice frame dramatically reduces the amount of frost growing on the window, such that the dots are still relatively clear. Interestingly, the ice frame strongly outperformed the nitrogen purge in terms of frost prevention. This implies that simply prewetting the frame of the

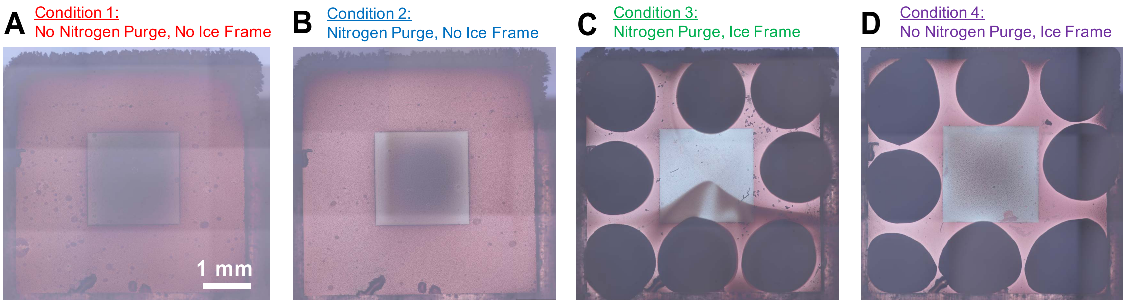

Figure 3. Bright-field microscopy of a silicon nitride window and frame under different conditions. Nine images taken with a 5× objective were stitched together to visualize the entire window and frame after 3 h of cryomicroscopy for each of the four conditions (A–D). The addition of an ice frame drastically improved the vibrancy and visual quality of the sample membrane surface at the center of the frame. Imaging of the ice frame also enabled the measurement of the annular dry zones of the frozen droplets.

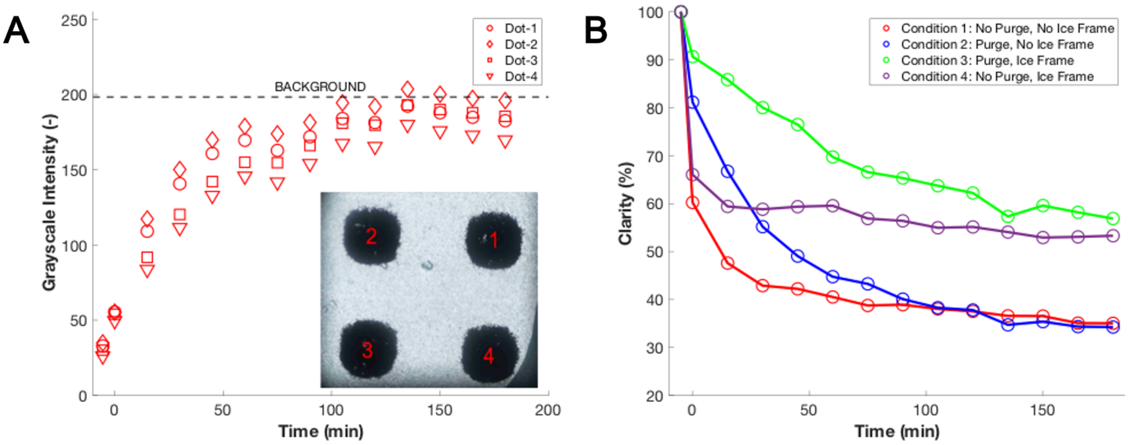

Figure 4. Quantifying the clarity of the dot arrays. (A) Grayscale intensity measurements for the black dot array on the white paper vs time. Measurements were taken every 15 min over 3 h of cryomicroscopy. The example plotted here was a trial under condition 1 (no purge and no ice frame); three trials were performed for each of the four conditions. (B) Extrapolation of the percentage clarity of the features versus time through a logarithmic expression. The figure shows that the conditions with the ice frame present had the greatest retention of clarity after a 3 h period.

sample window may be an inexpensive approach to combat frost accumulation.

Figure 3 shows a zoomed-out image of the entire silicon nitride window and surrounding ice frame for each of the four conditions after 3 h on the cryostage. For conditions 3 and 4, it can be seen that annular dry zones extend about the perimeter of each ice droplet on the ice frame, which confirms that the hygroscopic ice droplets attract water vapor from the environment. These dry zones were approximately $\delta_F = 90 \pm 30$ μm in width for condition 3 (purge) and $\delta_F = 105 \pm 14$ μm for condition 4 (no purge). It can also be seen that dry zones extend about each of the frost crystals that nucleate on the viewing window, for the equivalent reason that the frost is also hygroscopic. It should be noted that the temperature of the silicon nitride window is not uniform on the cryostage. For the conditions without a nitrogen purge, this is evident by the higher density of frost on the side of the window nearest the cold finger, especially when using an ice frame. The frost formation is more uniform in the presence of a nitrogen purge, as the convective flow can simultaneously make the window temperature more uniform and modify the transport of water vapor to the surface (i.e., no longer purely diffusive).

Quantitatively, the clarity of the underlying dot array is given by

$$\text{clarity} = 1 - \log_{10}\left[\frac{\left(\frac{I_d(t)}{I_b(t)}\right)}{\left(\frac{I_{d_0}}{I_{b_0}}\right)}\right] \quad (1)$$

where I_d (t) and I_b (t) are the average grayscale intensities of the dots and intermediate background, respectively, at any given time during cryoimaging, whereas I_{d_0} and I_{b_0} are the intensities of the dots and background at room temperature in the absence of frost, respectively (Supporting Figure S2). An example of measuring the grayscale intensity of the dots and background over time is shown in Figure 4A (for condition 1), which enables the calculation of the clarity using eq (1). As frost accumulates above the dots over time, it lightens their hue, causing their grayscale intensity to increase. As the difference between the grayscale intensity for the features and the background gets smaller, they begin to appear indistinguishable from each other.

The clarity as a function of time is plotted in Figure 4B for all four conditions. As expected, the clarity of experimental condition 1 (no purge and no ice frame) was overall the worst of any trial, dropping almost instantaneously from 100 to 60%. After decreasing further to a clarity of about 40% after about 30 min, the subsequent decrease in clarity over the next 3 hours was much more gradual, slowly progressing down to 35% by 3 h.

Condition 2 (purge and no ice frame) exhibited a more gradual decrease in clarity, requiring about 100 min to drop to a clarity of 40%. However, upon reaching a 40% clarity, the same trend was observed of a very slow decrease from that time on. This abrupt slowing in the rate of change of the clarity around 40% is likely because the frost crystals that had accumulated on the window were sufficiently dense to promote dry zones between them. In other words, after a critical amount of frost formation, only the pre-existing ice crystals grow, as opposed to nucleating fresh ice crystals in the remaining dry regions. As this coarsening is primarily out-of-plane as opposed to in-plane, it does not have as strong an effect on the clarity of the window.

For condition 3 (no purge and ice frame), the plateau occurred at around 60% clarity rather than 40%, such that the clarity was still over 50% after 3 h. This increase in the clarity's plateau value is because the ice frame itself is attracting the majority of the water vapor in the environment, such that the humidity directly over the window itself is smaller to enable dry zones at a smaller density of frost crystals.

For condition 4, the purge and ice frame work together to enable a maximal clarity of 80% after 30 min. The clarity does not drop down to 60% until after the full 3 h of time had elapsed, such that this condition was only beginning to reach the plateau value of clarity by the end of the experiment.

Dry Zone Measurement and Humidity Calculation. The frame's frozen droplets exhibited annular dry zones where frost growth was inhibited, as shown in Figure 3C,D. For a nitrogen-purged stage (condition 3), the annular width of each dry zone within 1 h of frost growth was $\delta_F = 90 \pm 30$ μm, whereas $\delta_F = 105 \pm 14$ μm in the absence of a purge (condition 4). Theoretically, the extent of a dry zone can be estimated by balancing the diffusive flux of water vapor at the edge of the dry zone. Specifically, at the periphery of the dry zone, the into-the-plane influx of water vapor from the ambient is equivalent to the lateral outflux of water vapor due to the nearby hygroscopic ice droplet.[18,21] This results in a flux dry zone of extent

$$\delta_F \sim \frac{\varsigma(c_w - c_i)}{c_\infty} \tag{2}$$

where ς is the out-of-plane thickness of the diffusive boundary layer, c_w and c_i are the saturation concentrations of (liquid) water and ice, respectively, and c_∞ is the concentration of water vapor in the ambient.

Here, the ambient humidity was too low to be measurable with our hygrometer. Considering that the δ_F values were measurable, we therefore decided to use eq 2 to solve for c_∞. The concentration boundary layer thickness (ς) is solved using the expression[27]

$$\varsigma \sim \left[\frac{D\varsigma_h^{3/2}}{4\sqrt{\alpha g(T_\infty - T_w)}}\right]^{1/3} \tag{3}$$

where D is the diffusivity of water vapor in air, α is the volumetric thermal expansion coefficient of air, T_w is the wall temperature of the silicon nitride window (and by extension, the frozen droplets), and ς_h is the hydrodynamic boundary layer approximated by

$$\varsigma_h \sim L_s\left(\frac{\alpha g(T_\infty - T_w)L_s^3}{\upsilon^2}\right)^{-1/5} \tag{4}$$

where $L_s \approx 2$ mm is the characteristic length of the membrane and υ is the kinematic viscosity of air.

The values of T_w and T_∞ differed when using a nitrogen purge (condition 3) vs no purge (condition 4). In the absence of a purge, the temperature of the silicon nitride window was $T_w \approx 95.15$ K, as measured by inserting a thermocouple into a droplet, frozen onto the window frame. The (relatively) warm nitrogen gas convectively heated the silicon nitride surface, resulting in a temperature of $T_w \approx 123.15$ K. The temperature of the chamber's ambient environment was measured to be approximately $T_\infty \approx 284.2$ K without the purge and $T_\infty \approx 281.6$ K with the purge. The nitrogen-purged and nonpurged chambers exhibited average gas pressures of 102.6 and 102.8 kPa, respectively (i.e., slightly above atmospheric pressure). From the ideal gas law, the concentrations can be found from

$$c_w = \frac{P_{sat,w}(T_w)}{RT_w},\ c_i = \frac{P_{sat,i}(T_w)}{RT_w},\ c_\infty = \frac{P_{sat,w}(T_\infty)RH}{RT_w} \tag{5}$$

where $R = 461.5$ J/(kg K) is the gas constant, $P_{sat,w}$ and $P_{sat,i}$ are the saturation pressures of liquid water and ice, respectively, as obtained from Murphy and Koop,[20] and RH is the relative humidity within the chamber. This resulted in $c_w = 2.92\text{e-}12$ kg/m^3 and $c_i = 8.81\text{e-}13$ kg/m^3 for the purged stage; for the nonpurged stage, $c_w = 3.31\text{e-}18$ kg/m^3 and $c_i = 6.65\text{e-}19$ kg/m^3.

When the chamber was purged with nitrogen gas, the hydrodynamic boundary layer thickness was calculated to be $\varsigma_h \sim 7.8\text{e-}4$ m (eq 4), resulting in a concentration boundary layer of $\varsigma \sim 2.5\text{e-}4$ m (eq 3). Combining eqs 2 and 5 together and using the averaged measurement of $\delta_F = 90$ μm, this results in an average chamber humidity of RH ~ 1.5e-4%. In the absence of a nitrogen purge, the calculated values of $\varsigma_h \sim 7.6\text{e-}4$ m and $\varsigma \sim 2.6\text{e-}4$ m, combined with the experimental average of $\delta_F = 105$ μm, resulted in RH ~ 1.8e-10%. In either case, the incredibly small humidity values explain why it could not be measured experimentally. It is also a testament to the perniciousness of the frost problem in the context of cryomicroscopy, as even minute concentrations of water vapor are able to nucleate on the surface due to its vanishing saturation pressure.

Biological Sample. In the next set of experiments, the dot array was removed, and a suspension of rat brain vessels was deposited on the surface of the silicon nitride window for cryomicroscopy. The vessels were isolated from the brains of a transgenic rat model (rTg-DI) of cerebral amyloid angiopathy.[28] The pathology of the cerebral blood vessels consisted of misfolded amyloid protein deposits (width: 3−4 μm) accumulated on the exterior of the blood vessels (width: 6−8 μm). The cerebral blood vessels were immunostained with collagen IV (red fluorescence), and the amyloid deposits were stained with thioflavin-S (green fluorescence).

Four different sets of images were produced for each vessel: two dark-field (red fluorescent protein (DsRed) and green fluorescent protein (GFP) filters; Figure 5A) and two bright-field (epi-illumination and transmission; see Supporting Figures S3 and S4). These images were taken using the same experimental conditions as the dot test and for an identical 3 h period. Aside from being consistent with the dot testing, maintaining these samples at low temperatures for prolonged (~h) test periods is important because biological tissues and microvessels are used in synchrotron-based X-ray fluorescence imaging[29−31] and cryopreservation is optimal to mitigate X-ray damage.[32,33] Depending on the resolution of the X-ray beam, sensitivity, and dwell time of the detector, extended intervals are required to perform an elemental analysis by raster scanning the specified area that comprise the mapped image of selected

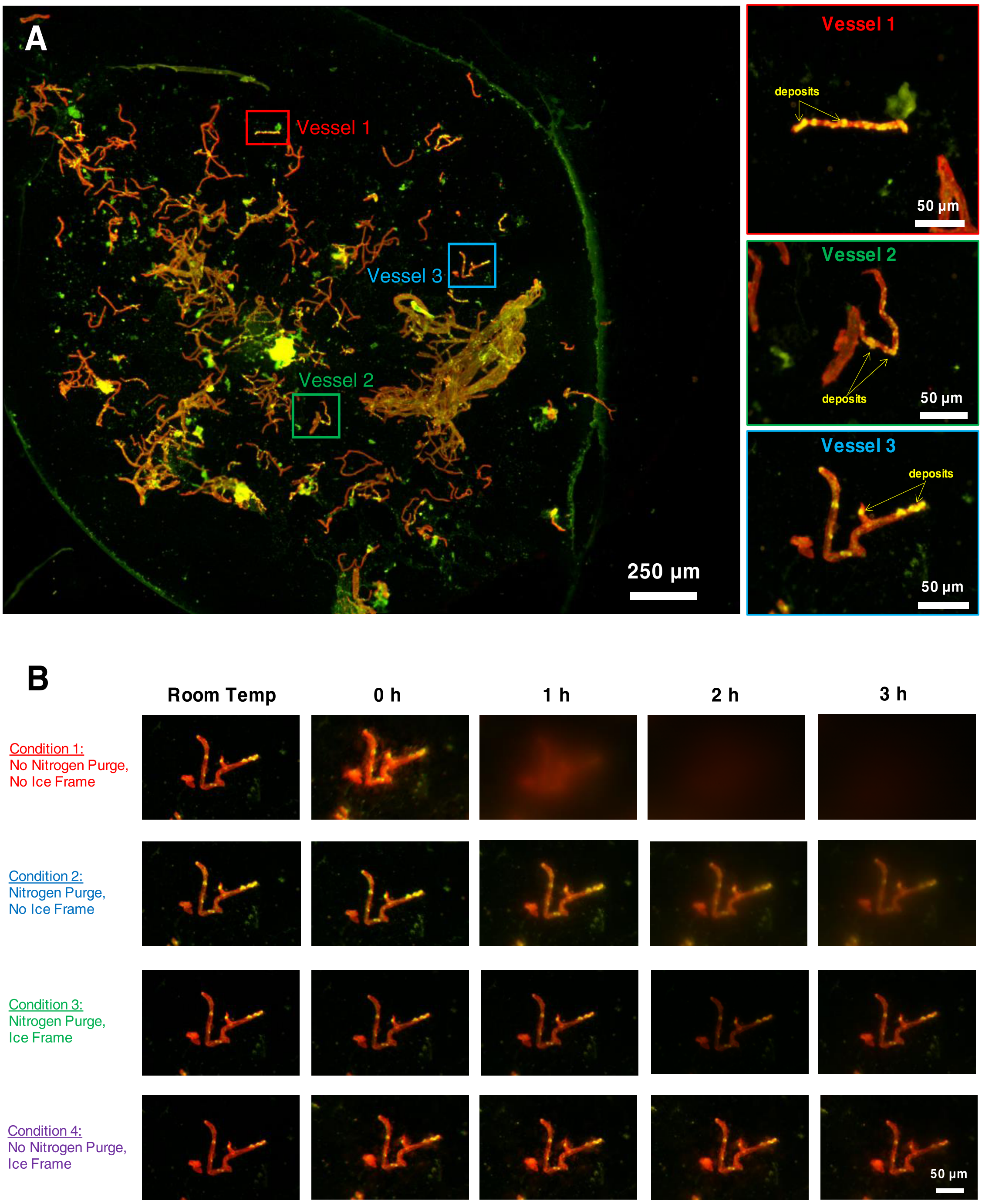

Figure 5. Using an ice frame improved cryomicroscopy of a biological specimen. Using dark-field illumination with red and green filters, fluorescently stained blood vessels containing amyloid deposits were placed on a silicon nitride window and imaged under a 50×/0.60 NA magnification. (A) Mosaic of the fluorescently stained biological sample, where microscopic images were stitched together and made into a composite by merging the red and green filtered images. This mosaic was captured at room temperature in the absence of any frost growth. Magnified insets depict the three microvessels chosen to evaluate the effectiveness of the ice frame in improving the clarity of fluorescence cryoimaging. (B) Time-lapse fluorescence microscopy of vessel 3 for each of the four conditions during cryomicroscopy. In conditions (2, 3) where the nitrogen purge was present, the substrate temperature was 123.15 K, while its absence in other conditions (1, 4) yielded a temperature of approximately 95.15 K. The fluorescence signal was almost completely lost after 3 h on the cryostage in the absence of an ice frame (top two rows), whereas the signal remained strong with an ice frame (bottom two rows). Images are composites of the microscope's DsRed and GFP filtered views.

vessels. For example, if the image of vessel 3 in Figure 5A was mapped using parameters (step size, 1 μm; dwell time, 0.15 s; and scan size, 100 μm × 100 μm), it would take 25 mins for that one vessel. Therefore, a 3 h test period is sufficient to not only map one vessel but also collect data from several.

For the dark-field images of the vessels, the presence of frost accumulation on the sample led to the fluorescent tags growing dimmer over time (Figure 5B). In the absence of an ice frame (conditions 1 and 2), the fluorescent tags were almost completely invisible after 3 h of cryomicroscopy. In contrast, when using an ice frame (conditions 3 and 4), fluorescence

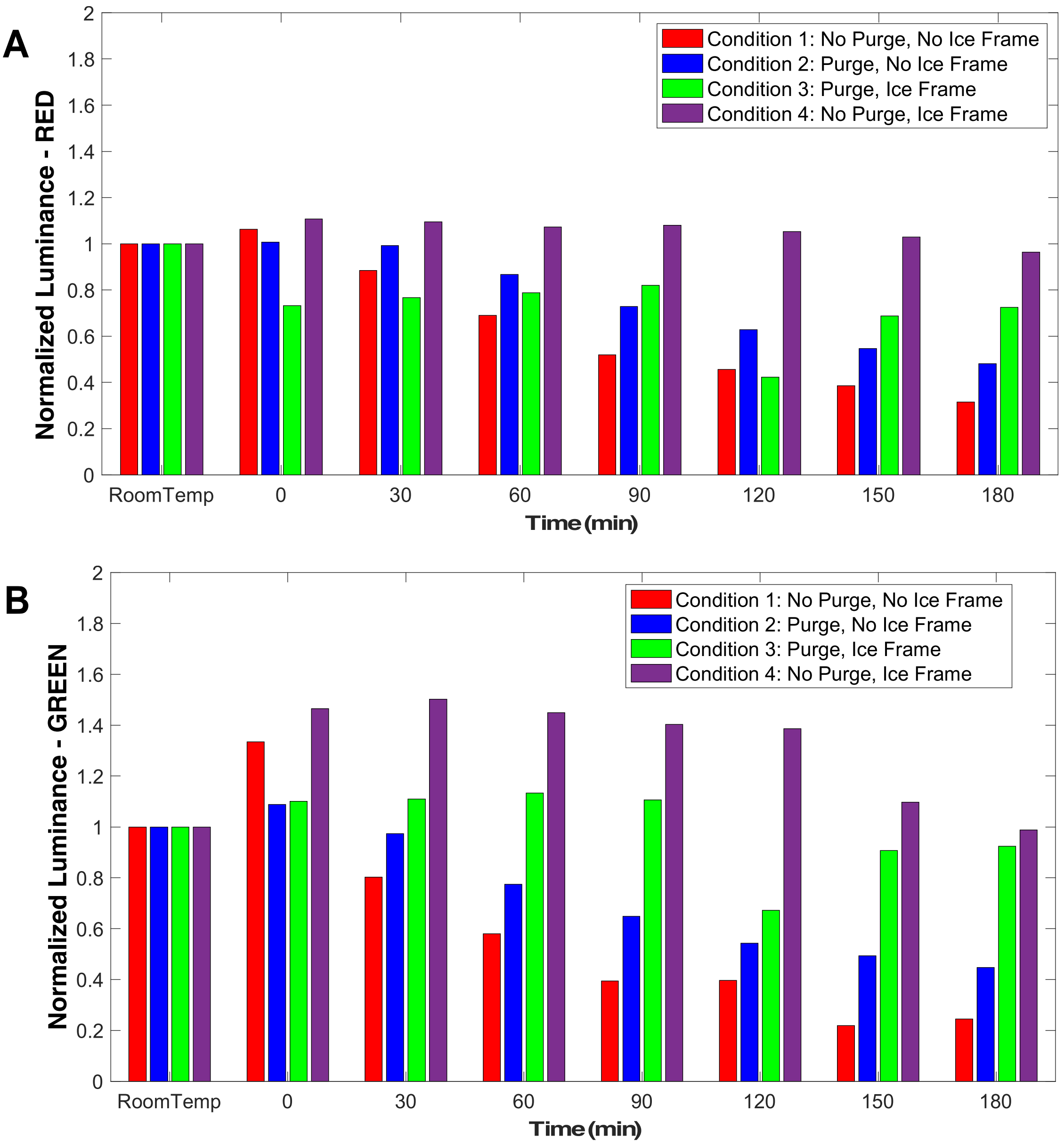

Figure 6. Average luminance of microvessel and amyloid deposits during fluorescence cryomicroscopy. The normalized luminescence of the collective vessels was measured every 30 min over 3 h of cryomicroscopy, for each of the four conditions, using (A) the DsRed filter for the red fluorescence (collagen IV) stained blood vessels (Supporting Figure S5) and (B) the GFP filter for the green fluorescence (thioflavin-S) stained amyloid deposits (Supporting Figure S6).

microscopy of the vessels was still robust after 3 h. Similarly, it was difficult to resolve the vessels in the bright-field images in the absence of the ice frame but were still visible when using the ice frame. These findings confirmed that the enhanced clarity in the presence of an ice frame can be extended to superior cryoimaging of a biological specimen.

Luminance of the pixels that comprised the selected vessels was initially measured on a scale of 0−100, every 30 min over a 3 h period of cryomicroscopy. After combining and averaging the pixel luminance values for all of the vessels, they were normalized against the luminance of the collective vessels at room temperature, readjusting the scale to 0−1.00. Changes in luminance were assessed to evaluate the loss of visibility due to frost. The normalized luminance at each 30 min timestamp is plotted in Figure 6 for all four test conditions.

To ensure quality control of the vessels while testing each of the conditions, at the beginning of every test, an image was taken of the vessels while they were being held at room temperature. Doing this at room temperature allowed for observations to be made, without gaseous product condensing on the sample surface. It was found that the average luminance of the vessels did not undergo any significant change, with a standard deviation of not more than 2 for every vessel. This finding suggested that the fluorescent tags on the vessels remained relatively undamaged in between testing the different conditions for 3 h periods, despite the frost accumulating on the vessel surface. This finding was to be expected, as cryogenic temperatures protect fluorescent tags from being washed out from photobleaching.[4,34]

With the DsRed filter, the observed luminescence of the vessels actually exceeded 1.00 for the first 30 min for condition 1 (no purge and no ice frame). The measured luminance then showed a drop at every 30 min interval, eventually reaching as low as 0.31 after 3 h. Condition 2 (purge and no ice frame) fared similarly, with the normalized luminance increasing marginally above 1.00 in early times and dropping down to only 0.48 after 3 h. We attribute lower initial luminance measure for condition 2 to the increased window temperature in the presence of a nitrogen flow, which seemed to remove the boost in luminescence achieved in condition 1. In contrast, the windows with ice frames performed substantially better, with a normalized luminance of 0.72 (condition 3, purge and ice frame) or 0.96 (condition 4, no purge and ice frame) after 3 h. However, the measured luminance for condition 3 experienced a steep decline at the starting (0 h) and 2 h timestamps before increasing in the succeeding intervals. Condition 3 was the last condition tested; it is possible that the fluctuations in luminescence are due to sample degradation after several days of repeated testing. The results were qualitatively similar for the GFP filter, except that in this case the luminescence for conditions 1 and 4 saw a significantly larger increase in their initial luminance measure at cryogenic temperatures, reaching 1.33 and 1.47, respectively. Cumulatively, these results indicated that a nitrogen purge diminished the fidelity of fluorescence cryomicroscopy, whereas the ice frame largely preserved the image quality even after 3 h of time.

Our results showed that immediately upon cooling down the biological sample to cryogenic temperatures, the measured luminance of the fluorescent tags attached to microvessels increased. This is consistent with what has been previously reported in fluorescent dyes and immunohistochemistry staining when held at cold temperatures.[4,5,35−37] In addition, mammalian cells have been noted to experience autofluorescence when held at cryogenic temperatures,[38,39] which may also contribute to heightened luminance. It is also worth noting that the luminescence yielded from the different immunohistochemistry staining was different at cryogenic temperatures, as thioflavin-S (green fluorescence) had higher luminance values than collagen IV (red fluorescence).

The initial increase in the luminance is believed to have contributed to their fluorescence images retaining their visibility longer than the bright-field images. After 3 h, the measured luminance was consistently highest for cases without the purge and with the ice frame for all microvessels. Without the presence of a convective flux from nitrogen purge, the sample is notably colder. This suggests an inverse relationship between temperature and luminance of the thioflavin-S and collagen IV. As time progressed, the calculated luminance decreased for every test case; however, the cases without the hygroscopic ice frame saw the greatest reduction in visibility of the stained microvessels.

■ DISCUSSION

In conclusion, we have shown that simply adding an ice frame to a silicon nitride window can significantly suppress frost growth for enhanced cryomicroscopy. While the dry zones encompassing the ice frame did not extend across the entire window, they depleted the concentration of water vapor such that the nucleation density of frost crystals was very low. Taking the fluorescence imaging of rat brain vessels as a prototypical example, the ice frame enhanced the vessel's luminescence by a factor of 6 compared to the conventional measure of a nitrogen purge. These results indicate that using a hygroscopic ice frame can substantially improve the clarity of cryomicroscopy while also being simpler than existing frost-fighting techniques.

Our results show that the ice frame performs well within an environment, mostly at atmospheric pressure, where the Brownian motion of the water vapor is expected to be primarily diffusive.[40] However, it is doubtful that these positive results would completely translate to systems where the vapor transport is ballistic, for example, within a vacuum environment.[41] Within a ballistic environment, the efficiency of the ice frame should decline due to reduction in the lateral motion of the water vapor molecules. It is suspected that the ice frame should still provide a notable degree of protection, but to what extent will need to be quantified through further testing.

Moving forward, it would be fruitful to develop a more continuous ice frame, that is, where water is wicked uniformly as opposed to deposited as discrete droplets. This would help boost the overall cumulative effect of the frame. Our decision to use droplets for this experiment was partially compelled due to the wettability of the frame, as untreated silicon nitride is fairly hydrophobic, making it difficult for the water to uniformly spread. But more so than that, droplets allow for the volume and height of the ice frame, relative to the sample on the window, to be independently varied to optimize the dryness of the sample. As evidenced by the work of Nath et al. 2018[21] and Ahmadi et al. 2018,[18] the overall height and volume of the frame contribute to its efficacy in collecting frost.

Before our ice frame concept can be practically applied, we encourage future research to systematically vary the dimensions of the ice frame, window frame, and interior window. As the silicon nitride window gets larger, we suspect that the increased area will make it increasingly more difficult for the ice frame to keep the sample dry. However, for the cryostage, the ice frame should still help deplete the water vapor in its sample chamber environment, as that volume remains fixed.

■ MATERIALS AND METHODS

Fabrication of Hygroscopic Silicon Nitride Windows. In this study, the sample substrate used for testing was a 5 mm × 5 mm silicon nitride window (Norcada/NX5200F, Alberta, Canada). Metal transmission electron microscopy (TEM) grids are typically chosen for cryoelectron microscopy (Cryo-EM) studies due to their robustness and thermal conductivity. Thin films, such as Kapton and especially Ultralene, offer high signal transmission, purity, and are frequently used as experimental surfaces for X-ray studies. For cryo-X-ray fluorescence microscopy, the frame of the silicon nitride window acts as a thermal conducting surface that can support the low temperatures for a frozen specimen,[42,43] with the additional benefit of its nitride membrane being an X-ray transparent, nonmetal support to avoid conflicting with the elemental detection of metals within the sample,[44,45] which would be an issue for TEM grids. Prior to testing, the silicon nitride windows were cleaned with oxygen plasma, with a mask placed over the central portion of the window where the supporting silicon was etched away. This created a nanoscale layer of hydrophilic silicon oxide (SiO_2) around the silicon-supported perimeter of the silicon nitride window.[46−48] This hydrophilic perimeter was then rendered hygroscopic by depositing eight 1.25 μL droplets of deionized water (four droplets on the corners and four between the corners) and freezing them into ice on the cryostage.

Operating the Cryostage. The silicon frame of the silicon nitride window was adhered, via epoxy, to one side of an aluminum holder and positioned so the silicon nitride membrane holding the sample (2 mm × 2 mm) fitted directly over the aperture of the holder. The window holder assembly was then cantilevered, with the window-side facing up, over the cooling block located within a custom cryogenic stage. The aluminum sample holder offsets the silicon nitride window from the cooling block, so that light avoids any background obstacles along its path as it transmits through the transparent silicon nitride membrane (Supporting Figures S7 and S8). The sample holder also serves as a conduit for thermal conduction between the block and the sample window.

The cryogenic stage was connected to a stage controller, a liquid nitrogen (LN2) pump, a water pump, and a liquid nitrogen dewar. For the experiments that utilized a hygroscopic frame, the top cryostage window was then removed to deposit the eight droplets of deionized (DI) water along the hydrophilic, nontransparent perimeter of the silicon nitride window. The cryostage window was then replaced, sealing the instrument, and the temperature of the cooling block was lowered to a few degrees below −273.15 K to freeze the droplets. Subsequently, the cooling block was chilled down to liquid nitrogen levels (77.15 K), the temperature level needed for cryomicroscopy. For a subset of the experiments, as the cooling block temperature dropped, nitrogen gas was circulated within the sample environment of the stage at a rate of 1.5 SCFH to reduce the humidity and purge most of the pre-existing condensable gases located within the stage chamber. The cryogenic stage was then placed under the optical microscope, and the silicon nitride window was brought into focus and white-balanced. The initial photos, once the cooling block of the cryogenic stage reached liquid nitrogen temperatures, were recognized as time zero ($t = 0$ min) for the experiments. Bright-field and/or fluorescence microscopy was then performed over a 3 h period for each sample as frost gradually accumulated on the window. The cryostage was then warmed back up to room temperature once testing was complete to allow the sample to dry.

Illuminated Dot Feature Array. For the first set of experiments, a small cutout of translucent film paper (Displays2go/LEDPPR8514, Fall River, MA) was glued to the reverse side of the silicon frame, opposite the silicon nitride window. This particular film paper was used because the way it diffused light on its reflecting surface appeared more Lambertian rather than specular, meaning it demonstrated a uniform luminance. The paper had an array of black dots (dia. ∼500 μm) printed on it, such that the features could be viewed through the transparent silicon nitride membrane (Supporting Figure S7). Before each test, while initially holding the stage at room temperature, a photo of the dot feature array and silicon nitride membrane was taken using the 5×/0.16 NA objective. Once the sample holder reached cryogenic levels, subsequent images of the dot array were taken over time as frost gradually accumulated on the silicon nitride window. Four different combinations of experimental conditions were tested: (1) nitrogen purge and no ice frame, (2) no purge and no ice frame, (3) no purge with an ice frame, and (4) purge with an ice frame. Cryoimaging was performed using each of the four experimental conditions.

The clarity of the dot array photos was obtained by taking ratios of the grayscale intensity of the dots versus the background at room temperature. A custom, intensity measuring computer program converted all of the photos taken from the black dot feature array test to grayscale over time (Supporting Figure S2 and the Supporting Materials). The grayscale conversion was used because any deposit of frost on the dots would cause the feature to lighten in hue.

Ice Frame Dry Zone Measurements. During the course of testing the dot array conditions with a hygroscopic ice frame, a mosaic image was created of the entire window under epi-illumination bright-field imaging using the 20×/0.80 NA objective. In those images, the ice frame is kept in focus so that the frozen droplets that comprise it and their encircling dry zones can be viewed. By employing the *Jahn5s/measuretool* function within MATLAB, the thickness of the dry zones could be estimated by measuring the distance from the frozen ice perimeter to the dry zone's boundary.[49]

Biological Specimen: Isolated Blood Vessels from rTg-DI Rats. In the second set of experiments, a biological specimen was imaged in place of the dot array. The biological specimen consisted of isolated cerebral blood vessels isolated from a transgenic rat model of cerebral amyloid angiopathy.[28] The blood vessels were tens of microns in length and a few microns in width and were isolated from the brains of 9 month old rTg-DI rats, as previously described.[50]

The isolated microvessels were deposited and dried onto the silicon nitride substrate and stained green with thioflavin-S (0.0125% in ethanol and phosphate-buffered saline) to visualize amyloid aggregates within the microvessels. A volume of 3 μL of the thioflavin-S was added to the isolated microvessels and incubated for 5 min. The stain was washed off using 70% ethanol. Immunohistochemistry staining was implemented to stain the microvessels red using rabbit polyclonal anticollagen IV primary antibodies (1:100) and incubated for 6 h. The samples were washed using phosphate-buffered saline (PBS) 3 times. Finally, the Alexa Fluor secondary antibody conjugates (1:1000) were added and incubated at room temperature for 3 h and washed 3 times using PBS to observe the microvessels.

After the biological specimen was prepared on the silicon nitride window, it was placed into the cryostage and cryoimaging was performed in the same manner as described above. The same three microvessels were identified and evaluated over a 3 h period for each of the four different sets of experimental conditions. The images of the microvessels were taken in 30 min intervals using four different optical microscopy illumination techniques: epi-illumination bright-field, transmission bright-field, and filtered dark-field illumination using settings for red (DsRed) and green (GFP). The DsRed fluorescent filter highlighted the immunostained (red) blood vessels, while the GFP fluorescent filter was used to illuminate the (green) amyloid deposits attached to them. All sets of images were taken at 50×/0.60 NA objective, with an accompanying 20×/0.40 NA mosaic of the entire membrane substrate taken at room temperature and each hour of cryogenic testing until completion.

To quantify the changes in clarity of the biological sample, a light measuring code was developed to convert the dark-field fluorescence images from their initial RGB color space to the CIELAB color space (Supporting Figure S9 and the Supporting Materials). The CIELAB color space is a three-dimensional space that includes luminance as one of its metrics.[51] The code averaged the luminance of the color images of the vessels after segmenting them out from the imported CIELAB image. Knowing the fluorescent tags can only attach themselves to the vessels, segmentation was accomplished using machine learning, via K-means clustering, to create two data clusters, one that represented the illuminated vessel and the other for background pixels. The average luminance measured was tabulated and used to monitor changes in the biological sample visibility. Evaluations were made from the average intensities as to the performance of each experimental condition[52] over time. Similar approaches have been documented by other researchers.[53]

ASSOCIATED CONTENT

Supporting Information

The Supporting Information is available free of charge at https://pubs.acs.org/doi/10.1021/acsomega.2c03083.

Microscopy of silicon nitride window during frost growth at cryogenic temperatures; grayscale intensity measurements of the dot feature array; epi-bright-field microscopy of isolated rat brain vessels with amyloid deposits; transmission bright-field microscopy of isolated rat brain vessels with amyloid deposits; dark-field fluorescent images (DsRed) of rat brain vessel 3 during 3 h of cryomicroscopy; dark-field fluorescent images (GFP) of rat brain vessel 3 during 3 h of cryomicroscopy; schematic of the experimental setup incorporating the dot array; schematic of the experimental setup; and image segmentation through k-means clustering (PDF)

Example of dot array clarity change over a 3 h period (MOV)

Luminance observation of rat brain vessel over a 3 h period (MOV)

Dot array test intensity measurements, and average luminance of the rat brain vessels (XLSX)

AUTHOR INFORMATION

Corresponding Author

Jonathan B. Boreyko − *Department of Mechanical Engineering, Virginia Tech, Blacksburg, Virginia 24060, United States;* orcid.org/0000-0003-0344-5868; Email: boreyko@vt.edu

Authors

Adam W. Lowery − *Department of Mechanical Engineering, Virginia Tech, Blacksburg, Virginia 24060, United States; National Synchrotron Light Source II, Brookhaven National Laboratory, Upton, New York 11973, United States;* orcid.org/0000-0001-9753-1614

Ashwin Ambi − *National Synchrotron Light Source II, Brookhaven National Laboratory, Upton, New York 11973, United States; Department of Chemistry, Stony Brook University, Stony Brook, New York 11794, United States*

Lisa M. Miller − *National Synchrotron Light Source II, Brookhaven National Laboratory, Upton, New York 11973, United States; Department of Chemistry, Stony Brook University, Stony Brook, New York 11794, United States;* orcid.org/0000-0002-2912-7991

Complete contact information is available at: https://pubs.acs.org/10.1021/acsomega.2c03083

Author Contributions

A.W.L. and J.B.B. conceived the study. A.W.L. and A.A. performed the experiments (under the supervision of J.B.B. and L.M.M.), and the biological materials were provided by L.M.M., A.W.L., and J.B.B. analyzed the results from the experiments. A.W.L., J.B.B., A.A., and L.M.M. wrote the manuscript.

Funding

This work was supported by the Center of BioMolecular Structure (CBMS). CBMS is primarily supported by the National Institutes of Health, the National Institute of General Medical Sciences (NIGMS), through a Center Core P30 Grant (P30GM133893), and by the DOE Office of Biological and Environmental Research (DOE-BER) (KP1607011). The Bio-Imaging Core within the CMBS was supported entirely by the DOE-BER.

Notes

The authors declare no competing financial interest.

The authors declare no competing interest at this moment. Data used to interpret the results are present in this paper and/or in the Supporting Materials. All raw data files may be available upon request. Codes used to process raw data may be available upon request. Inquiries should be addressed to A.W.L. at adamwl@vt.edu.

ACKNOWLEDGMENTS

This research used resources of the National Synchrotron Light Source II and the Center for Functional Nanomaterials (CFN), the Department of Energy (DOE) Office of Science User Facilities operated for the DOE Office of Science by Brookhaven National Laboratory under Contract No. DE-SC0012704. This work was also supported by the DOE Office of Biological and Environmental Research (KP1605010). We thank the Virginia Tech Open Access Subvention Fund (VT OASF) for covering the publication costs. The authors would like to thank Dr. Ming Lu, from CFN, for plasma cleaning of the silicon nitride windows to develop a silicon oxide layer on the window frame and increase the surface hydrophobicity and Dr. William E. Van Nostrand at the University of Rhode Island (Kingston, RI) for kindly supplying the cerebral isolated vessels from rTg-DI rats. A part of this work was supported by NIH grant NS094201 to Dr. William E. Van Nostrand and Dr. L.M.M. In addition, the authors would like to thank Dr. Ryan V. Tappero and Randy J. Smith for helping to secure funding for this research and supplying the cryostage.

REFERENCES

(1) Dubochet, J.; LePault, J.; Freeman, R.; Berriman, J. A.; Homo, J.-C. Electron microscopy of frozen water and aqueous solutions. *J. Microsc.* **1982**, *128*, 219−237.

(2) Dubochet, J.; Blanc, N. S. The cell in absence of aggregation artifacts. *Micron* **2001**, *32*, 91−99.

(3) Li, Y.; Almassalha, L. M.; Chandler, J. E.; Zhou, X.; Stypula-Cyrus, Y. E.; Hujsak, K. A.; Roth, E. W.; Bleher, R.; Subramanian, H.; Szleifer, I.; et al. The effects of chemical fixation on the cellular nanostructure. *Exp. Cell Res.* **2017**, *358*, 253−259.

(4) Schwartz, C. L.; Sarbash, V. I.; Ataullakhanov, F. I.; Mcintosh, J. R.; Nicastro, D. Cryo-fluorescence microscopy facilitates correlations between light and cryo-electron microscopy and reduces the rate of photobleaching. *J. Microsc.* **2007**, *227*, 98−109.

(5) Kaufmann, R.; Hagen, C.; Grunewald, K. Fluorescence cryo-microscopy: current challenges and prospects. *Curr. Opin. Chem. Biol.* **2014**, *20*, 86−91.

(6) Salomé, M.; Cotte, M.; Baker, R.; Barrett, R.; Benseny-Cases, N.; Berruyer, G.; Bugnazet, D.; Castillo-Michel, H.; Cornu, C.; Fayard, B.; et al. The ID21 Scanning X-ray Microscope at ESRF. *J. Phys.: Conf. Ser.* **2013**, *425*, No. 182004.

(7) Chen, S.; Deng, J.; Yuan, Y.; Flachenecker, C.; Mak, R.; Hornberger, B.; Jin, Q.; Shu, D.; Lai, B.; Maser, J.; et al. The Bionanoprobe: hard X-ray fluorescence nanoprobe with cryogenic capabilities. *J. Synchrotron Radiat.* **2014**, *21*, 66−75.

(8) Tuijtel, M. W.; Koster, A. J.; Jakobs, S.; Faas, F. G. A.; Sharp, T. H. Correlative cryo super-resolution light and electron microscopy on mammalian cells using fluorescent proteins. *Sci. Rep.* **2019**, *9*, No. 1369.

(9) Apkarian, R. P. Cryo-Temperature Stages in Nanostructural Research. In *Scanning Microscopy for Nanotechnology: Techniques and Applications*; Spring Street: New York, 2006; Vol. *233*, pp 467−489.

(10) Dubochet, J.; Adrian, M.; Chang, J.-J.; Homo, J. C.; Lepault, J.; McDowall, A. W.; Schultz, P. Cryo-Electron Microscopy of Vitrified Specimens. *Q. Rev. Biophys.* **1988**, *21*, 129−228.

(11) Capaccioli, S.; Ngai, K. L. Resolving the controversy on the glass transition temperature of water? *J. Chem. Phys.* **2011**, *135*, No. 104504.

(12) Amann-Winkel, K.; Gainaru, C.; Handle, P. H.; Seidl, M.; Nelson, H.; Böhmer, R.; Loerting, T. Water's second glass transition. *Proc. Natl. Acad. Sci. U.S.A.* **2013**, *110*, 17720−17725.

(13) Fourcade, M. C. M.; Barnola, J. M.; Susini, J.; Baker, R.; Durand, G.; de Angelis, M.; Duval, P. Application of micro-X-ray fluorescence to chemical mapping of polar ice. *J. Glaciol.* **2005**, *51*, 325−332.

(14) van Driel, L. F.; Valentijn, J. A.; Valentijn, K. M.; Koning, R. I.; Koster, A. J. Tools for correlative cryo-fluorescence microscopy and cryo-electron tomography applied to whole mitochondria in human endothelial cells. *Eur. J. Cell Biol.* **2009**, *88*, 669−684.

(15) Arnold, J.; Mahamid, J.; Lucic, V.; de Marco, A.; Fernandez, J.-J.; Laugks, T.; Mayer, T.; Hyman, A.; Baumeister, W.; Plitzko, J. Site-Specific Cryo-focused Ion Beam Sample Preparation Guided by 3D Correlative Microscopy. *Biophys. J.* **2016**, *110*, 860−869.

(16) Dent, K. C.; Hagen, C.; Grünewald, K. Critical Step-by-Step Approaches Toward Correlative Fluorescence/Soft X-Ray Cryo-Microscopy of Adherent Mammalian Cells. In *Methods in Cell Biology*, Müller-Reichert, T.; Verkade, P., Eds.; Academic Press, 2014; Vol. *124*, pp 179−216.

(17) Hampton, C. M.; Strauss, J. D.; Ke, Z.; Dillard, R. S.; Hammonds, J. E.; Alonas, E.; Desai, T. M.; Marin, M.; Storms, R. E.; Leon, F.; et al. Correlated fluorescence microscopy and cryo-electron tomography of virus-infected or transfected mammalian cells. *Nat. Protoc.* **2017**, *12*, 150−167.

(18) Ahmadi, S. F.; Nath, S.; Iliff, G. J.; Srijanto, B. R.; Collier, C. P.; Yue, P.; Boreyko, J. B. Passive Antifrosting Surfaces Using Microscopic Ice Patterns. *ACS Appl. Mater. Interfaces* **2018**, *10*, 32874−32884.

(19) Edgar, G.; Swan, W. O. The Factors Determining The Hygroscopic Properties Of Soluble Substances. I. The Vapor Pressures Of Saturated Solutions. *J. Am. Chem. Soc.* **1922**, *44*, 570−577.

(20) Murphy, D. M.; Koop, T. Review of the vapour pressures of ice and supercooled water for atmospheric applications. *Q. J. R. Meteorol. Soc.* **2005**, *131*, 1539−1565.

(21) Nath, S.; Bisbano, C.; Yue, P.; Boreyko, J. Duelling dry zones around hygroscopic droplets. *J. Fluid Mech.* **2018**, *853*, 601−620.

(22) De Koninck, L. H.; Ahmadi, S. F.; Boreyko, J. B. Passive anti-frosting cables. *Int. J. Heat Mass Transfer* **2020**, *146*, No. 118808.

(23) Huang, X.; Miao, H.; Nelson, J.; Turner, J.; Steinbrener, J.; Shapiro, D.; Kirz, J.; Jacobsen, C. Anti-contamination device for cryogenic soft X-ray diffraction microscopy. *Nucl. Instrum. Methods Phys. Res., Sect. A* **2011**, *638*, 171−175.

(24) Tacke, S.; Krzyzanek, V.; Nüsse, H.; Wepf, R. A.; Klingauf, J.; Reichelt, R. A Versatile High-Vacuum Cryo-transfer System for Cryo-microscopy and Analytics. *Biophys. J.* **2016**, *110*, 758−765.

(25) Li, S.; Ji, G.; Shi, Y.; Klausen, L. H.; Niu, T.; Wang, S.; Huang, X.; Ding, W.; Zhang, X.; Dong, M.; et al. High-vacuum Optical Platform for cryo-CLEM (HOPE): a New Solution for Non-integrated Multiscale Correlative Light and Electron Microscopy. *J. Struct. Biol.* **2017**, *201*, 63−75.

(26) Walker, C.; Mitridis, E.; Kreiner, T.; Eghlidi, H.; Schutzius, T. M.; Poulikakos, D. Transparent Metasurfaces Counteracting Fogging by Harnessing Sunlight. *Nano Lett.* **2019**, *19*, 1595−1604.

(27) Medici, M.-G.; Mongruel, A.; Royon, L.; Beysens, D. Edge effects on water droplet condensation. *Phys. Rev. E* **2014**, *90*, No. 062403.

(28) Davis, J.; Xu, F.; Hatfield, J.; Lee, H.; Hoos, M. D.; Popescu, D.; Crooks, E.; Kim, R.; Smith, S. O.; Robinson, J. K.; et al. A Novel Transgenic Rat Model of Robust Cerebral Microvascular Amyloid with Prominent Vasculopathy. *Am. J. Pathol.* **2018**, *188*, 2877−2889.

(29) Bourassa, M. W.; Leskovjan, A. C.; Tappero, R. V.; Farquhar, E. R.; Colton, C. A.; Van Nostrand, W. E.; Miller, L. M. Elevated copper in the amyloid plaques and iron in the cortex are observed in mouse models of Alzheimer's disease that exhibit neurodegeneration. *Biomed. Spectrosc. Imaging* **2013**, *2*, 129−139.

(30) Jin, Q.; Paunesku, T.; Lai, B.; Gleber, S. C.; Chen, S. I.; Finney, L.; Vine, D.; Vogt, S.; Woloschak, G.; Jacobsen, C. Preserving elemental content in adherent mammalian cells for analysis by synchrotron-based x-ray fluorescence microscopy. *J. Microsc.* **2017**, *265*, 81−93.

(31) Kopittke, P. M.; Punshon, T.; Paterson, D. J.; Tappero, R. V.; Wang, P.; Blamey, F. P. C.; van der Ent, A.; Lombi, E. Synchrotron-Based X-Ray Fluorescence Microscopy as a Technique for Imaging of Elements in Plants. *Plant Physiol.* **2018**, *178*, 507−523.

(32) Bissardon, C.; Isaure, M.-P.; Lesuisse, E.; Rovezzi, M.; Lahera, E.; Proux, O.; Bohic, S. Biological Samples Preparation for Speciation at Cryogenic Temperature using High-Resolution X-Ray Absorption Spectroscopy. *J. Visualized Exp.* **2022**, No. e60849.

(33) Meents, A.; Gutmann, S.; Wagner, A.; Schulze-Briese, C. Origin and temperature dependence of radiation damage in biological samples at cryogenic temperatures. *Proc. Natl. Acad. Sci. U.S.A.* **2010**, *107*, 1094−1099.

(34) Tytus, B.; Bartlomiej, P. R.; Elikplimki, K. A.; Joseph Paul, R. Loss of image quality in photobleaching during microscopic imaging of fluorescent probes bound to chromatin. *J. Biomed. Opt.* **2005**, *10*, No. 064015.

(35) Zondervan, R.; Kulzer, F.; Kol'chenk, M. A.; Orrit, M. Photobleaching of Rhodamine 6G in Poly(vinyl alcohol) at the Ensemble and Single-Molecule Levels. *J. Phys. Chem. A* **2004**, *108*, 1657−1665.

(36) Hawe, A.; Sutter, M.; Jiskoot, W. Extrinsic Fluorescent Dyes as Tools for Protein Characterization. *Pharm. Res.* **2008**, *25*, 1487−1499.

(37) Hulleman, C. N.; Li, W.; Gregor, I.; Rieger, B.; Enderlein, J. Photon Yield Enhancement of Red Fluorophores at Cryogenic Temperatures. *ChemPhysChem* **2018**, *19*, 1774−1780.

(38) Benson, R. C.; Meyer, R. A.; Zaruba, M. E.; McKhann, G. M. Cellular autofluorescence–is it due to flavins? *J. Histochem. Cytochem.* **1979**, *27*, 44−48.

(39) Carter, S. D.; Mageswaran, S. K.; Farino, Z. J.; Mamede, J. I.; Oikonomou, C. M.; Hope, T. J.; Freyberg, Z.; Jensen, G. J. Distinguishing signal from autofluorescence in cryogenic correlated light and electron microscopy of mammalian cells. *J. Struct. Biol.* **2018**, *201*, 15−25.

(40) Liu, D.-L. Particle Deposition onto Enclosure Surfaces. In *Developments in Surface Contamination and Cleaning*, Kohli, R.; Mittal, K. L., Eds.; William Andrew Publishing, 2010; pp 1−56.

(41) Li, T.; Kheifets, S.; Medellin, D.; Raizen, M. Measurement of the Instantaneous Velocity of a Brownian Particle. *Science* **2010**, *328*, 1673−1675.

(42) Tanner, J. R.; Demmert, A. C.; Dukes, M. J.; Melanson, L. A.; McDonald, S. M.; Kelly, D. F. Cryo-SiN − An Alternative Substrate to Visualize Active Viral Assemblies. *J. Anal. Mol. Tech.* **2013**, *1*, No. 6.

(43) Bissardon, C.; Reymond, S.; Salome, M.; Andre, L.; Bayat, S.; Cloetens, P.; Bohic, S. Cell Culture on Silicon Nitride Membranes and Cryopreparation for Synchrotron X-ray Fluorescence Nano-analysis. *J. Visualized Exp.* **2019**, No. e60461.

(44) Ralle, M.; Lutsenko, S. Quantitative imaging of metals in tissues. *BioMetals* **2009**, *22*, 197−205.

(45) Bourassa, M. W.; Miller, L. M. Metal imaging in neurodegenerative diseases. *Metallomics* **2012**, *4*, 721−738.

(46) Liu, L.; Michalak, D.; Chopra, T.; Pujari, S.; Cabrera, W.; Dick, D.; Veyan, J.-F.; Hourani, R.; Halls, M.; Zuilhof, H.; et al. Surface etching, chemical modification and characterization of silicon nitride and silicon oxide - Selective functionalization of Si3N4 and SiO2. *J. Phys.: Condens. Matter* **2015**, *28*, No. 094014.

(47) Saengdee, P.; Chaisriratanakul, W.; Bunjongpru, W.; Sripumkhai, W.; Srisuwan, A.; Jeamsaksiri, W.; Hruanun, C.; Poyai, A.; Promptmas, C. Surface modification of silicon dioxide, silicon nitride and titanium oxynitride for lactate dehydrogenase immobilization. *Biosens. Bioelectron.* **2015**, *67*, 134−138.

(48) Usenko, A.; Senawiratne, J. Silicon Nitride Surface Conversion into Oxide to Enable Hydrophilic Bonding. *ECS Trans.* **2010**, *33*, 475−483.

(49) Jann5s/measuretool; Mathworks: MATLAB Central, 2021. https://github.com/Jann5s/measuretool (accessed May 24, 2021).

(50) Zlokovic, B. V.; Mackic, J. B.; Wang, L.; McComb, J. G.; McDonough, A. Differential expression of Na,K-ATPase alpha and beta subunit isoforms at the blood-brain barrier and the choroid plexus. *J. Biol. Chem.* **1993**, *268*, 8019−8025.

(51) Luo, M. R. CIELAB. In *Encyclopedia of Color Science and Technology*, Luo, M. R., Ed.; Springer: New York, 2016; pp 207−212.

(52) Wang, H.; Cuijpers, R.; Luo, M.; Heynderickx, I.; Zheng, Z. Optimal illumination for local contrast enhancement based on the human visual system. *J. Biomed. Opt.* **2015**, *20*, No. 015005.

(53) Baldevbhai, P. J. Color Image Segmentation for Medical Images using L*a*b* Color Space. *IOSR J. Electron. Commun. Eng.* **2012**, *1*, 24−45.